

Chapter 5

3D Gulf of Mexico data example

In this chapter, I apply joint least-squares reverse time migration (joint LSRTM) to a synthetic three-dimensional ocean-bottom node (OBN) dataset. The model used to generate the synthetic data is based on the Deimos dataset in Chapter 3. The dataset is designed to simulate a range of imaging challenges in the Gulf of Mexico. Instead of using traditional ocean-bottom node acquisition geometry, I used a pseudo-random distribution of ocean-bottom receivers. Despite the fact that relatively few OBN receivers are used in the survey, joint LSRTM can still generate a relatively well-illuminated subsurface image when higher-order surface related multiples are included in imaging.

To speed up the rate of convergence, I have applied some of the techniques introduced in Chapter 3. One technique addresses the issue of shadow zones in the subsurface due to a complex salt structure. To emphasize deeper parts of the image near the salt, I use a target-oriented data-reweighting in least-squares reverse-time migration. To extract the most information from the LSRTM algorithm with the fewest number of iterations, I include salt dimming in the inversion.

I will begin by introducing the 3D synthetic dataset. I will then describe some of the processing and workflow applied before running migration. I will show some of the reverse time migration (RTM) and LSRTM results using different modes of

reflection data as operators. The joint LSRTM algorithm can properly combine the information from first and higher order surface-related multiples energy. Compared to using only the first order reflection, I will show that joint LSRTM can provide crosstalk noise reduction and illumination improvement in the image.

3D SYNTHETIC GULF OF MEXICO MODEL

This synthetic model is created by Robert Clapp which is based on a user specified sequence of geological events (Clapp, 2014). The salt structure in this dataset is modeled after the salt structure from the Deimos field dataset from Chapter 3. The model contains various geological features including deformation, folds, faults, and planes. Some unconventional structures are also included to test the capability of my imaging algorithms. The goal is to create many areas that are difficult to image using tradition migration. In particular, I am interested in seeing how different imaging processes will perform in shadow zones. Figure 5.1a shows the velocity profile used to create the synthetic data. As part of the blind test, I do not have access to the true velocity mode. Instead, some errors were introduced to the migration velocity model for the subsequent migration and LSRTM calculation. Figure 5.1b shows the velocity error (in percents) between the migration velocity and the true velocity. Negative errors mean that the migration velocity is underestimated while positive errors mean that the migration velocity is overestimated. The errors in the migration velocity model are clustered in several regions and deviate as much as 20% from the true velocity model.

The depth of the model is 7km, with a lateral size of 13.5km x 13.5km. The datasets are then simulated using the Born forward modeling method and the constant-density acoustic wave equation.

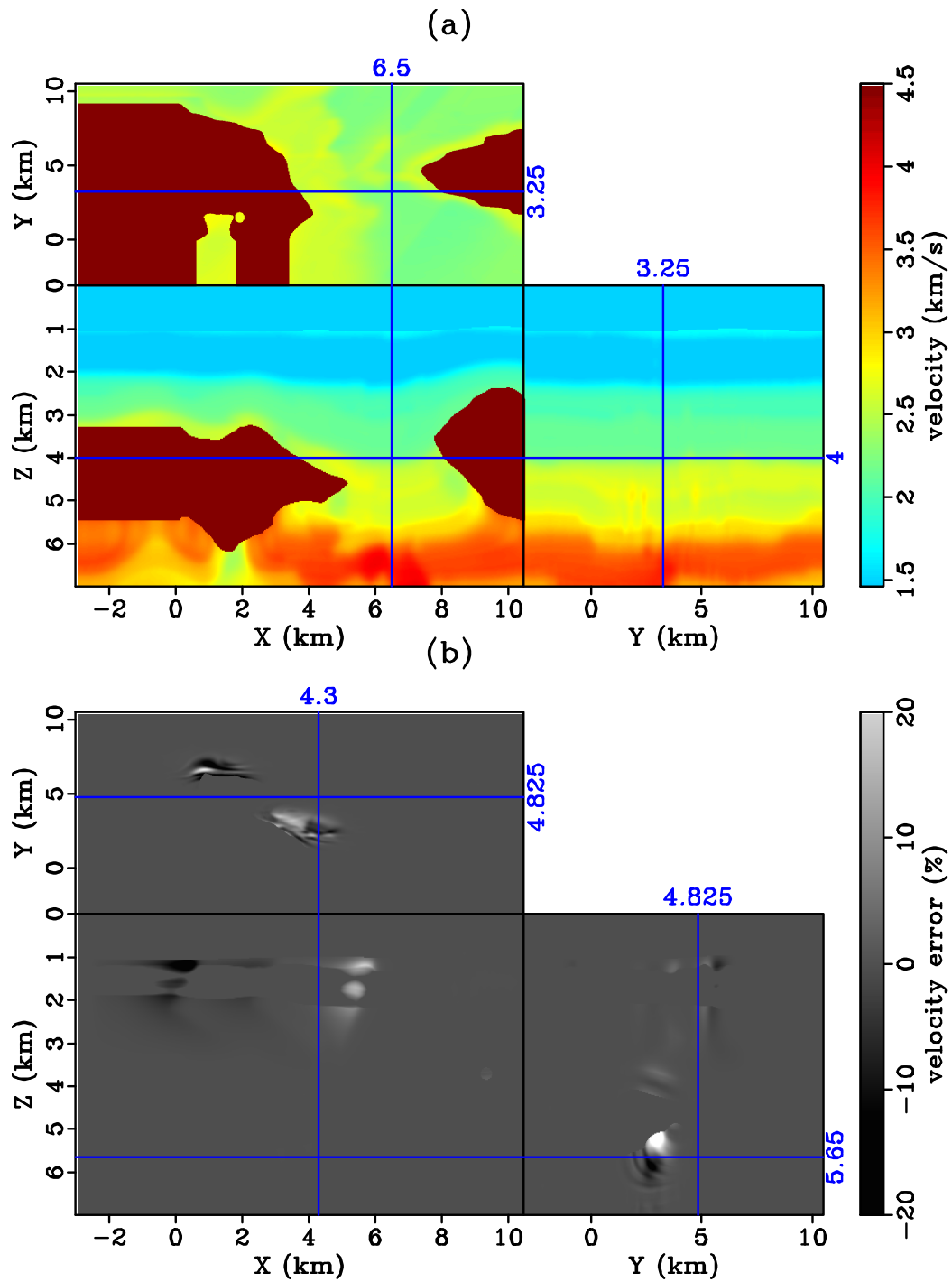


Figure 5.1: (a) Velocity model used to generate the synthetic data. (b) Velocity error (in percent) in the migration velocity model. [ER] chap5/. chap5-fig1-velSyn3D

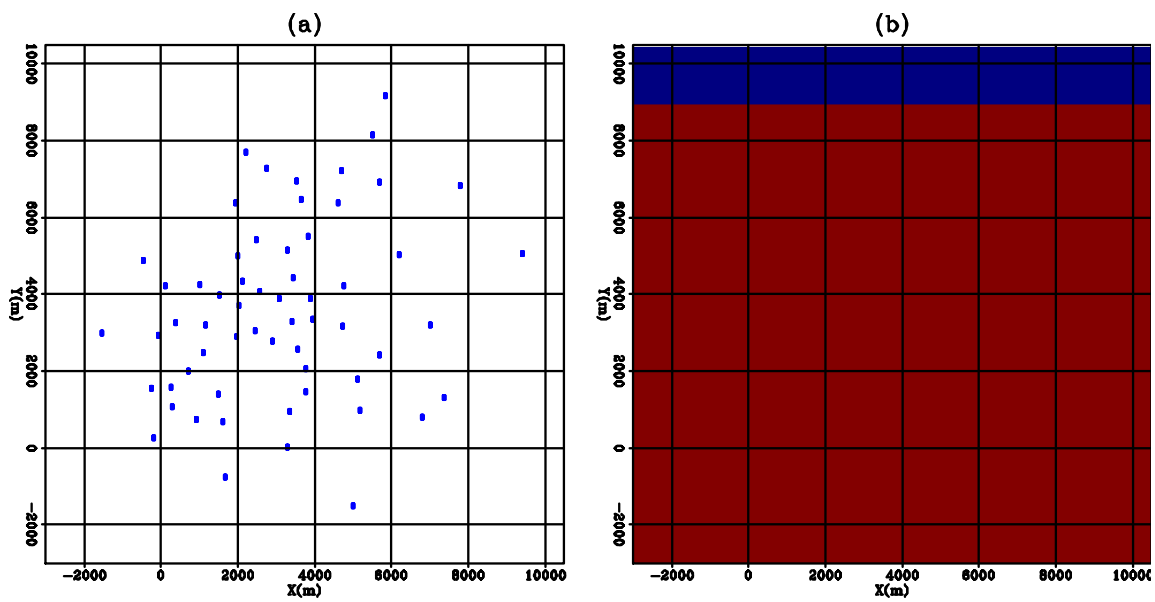


Figure 5.2: The study area is 13.5km x 13.5km wide in both the inline (x) and crossline (y) directions. (a) shows the distribution of ocean-bottom nodes for this survey. A total of 60 nodes are used. (b) shows the location of the physical shots in red. The shot spacing is 25m in both inline and crossline directions. [ER]

chap5/. chap5-geom

Acquisition geometry

We use the ocean-bottom node acquisition geometry for this dataset to generate different order of reflection arrivals. In practice, the data are simulated per receiver gather using reciprocity, in which the role of the shots and receivers are exchanged. An unconventional distribution of ocean-bottom nodes is used instead of a traditional spreading of OBN nodes. The industry standard typically has a node spacing of 400m and the OBNs are distributed in either a rectangular or hexagonal grid. The rectangular or hexagonal grid is centered at the target region. In this dataset, we employ node spacing that are at least 400m; the nodes are distributed in a pseudo-random fashion with higher density in the target region. The nodes are then gradually spaced further apart. Figure 5.2a shows the distribution of the 60 OBNs in this synthetic dataset. This type of distribution allows us to simulate with far fewer receivers. In an actual field acquisition, this will translate into shorter acquisition time.

Synthetic dataset

For this dataset, we simulate the pressure wavefield directly using Born forward modeling. To verify the theory discussed in Chapter 4, I will be studying the contribution from the first two orders of down-going reflection (Figure 5.3). For simplicity, I will refer to the first order of down-going reflection (Figure 5.3a) as the mirror reflection. The second order of down-going reflection (Figure 5.3b) will be called the double-mirror reflection.

To generate the mirror reflection, we used the procedure described in Figure 4.2 where the OBN node is placed at the mirror position with respect to the sea surface. We used the procedure in Figure 4.3 to generate the double-mirror reflection. Figure 5.4a and 5.4b show a receiver gather with mirror-only reflection and double-mirror only reflection. The sum of the two modes (Figure 5.4c) should adequately represent the total down-going energy as higher order surface-related multiples will become

gradually weaker. The pressure data are simulated per receiver gather using reciprocity, in which the role of the shots and receivers are exchanged. Figure 5.2b shows the distribution of the shot carpet (in red) for this survey. The shots are spaced 25m apart in both the inline and the crossline directions.

Since the data are prepared synthetically, a minimal amount of pre-processing is needed. One pre-processing step I made was to apply static time shifts in the OBN gather to move the dataset from a grid of 12.5m sampling to 25m sampling. I found that this provide sufficient correction.

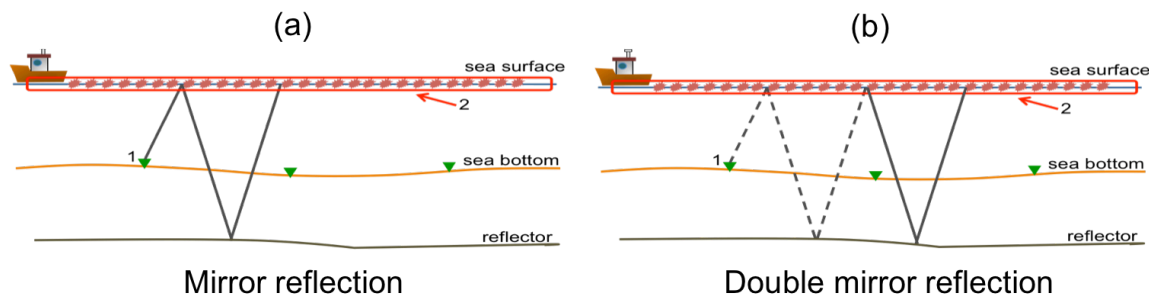


Figure 5.3: (a) The first-order of down-going reflection. It will be referred to as the mirror reflection. (b) The second-order of surface-related down-going reflection. It will be referred to as the double reflection. [NR] chap5/. MirrorDoubleRay

MIRROR LSRTM AND JOINT LSRTM

I ran two LSRTMs with the down-going data, containing both the mirror and the double-mirror arrival. The first inversion has an operator that only accounts for the kinematics of the mirror reflection. Its objective function, $S_{\text{mirror}}(\mathbf{m})$, is:

$$S_{\text{mirror}}(\mathbf{m}) = \|\mathbf{L}_{\text{mirror}}\mathbf{m} - \mathbf{d}_\downarrow\|^2, \quad (5.1)$$

where $\mathbf{L}_{\text{mirror}}$ represents the Born forward modeling operator for the mirror reflection, and \mathbf{m} is the image model. The down-going data, \mathbf{d}_\downarrow , (Figure 5.4c) contain both the mirror and the double-mirror reflection.

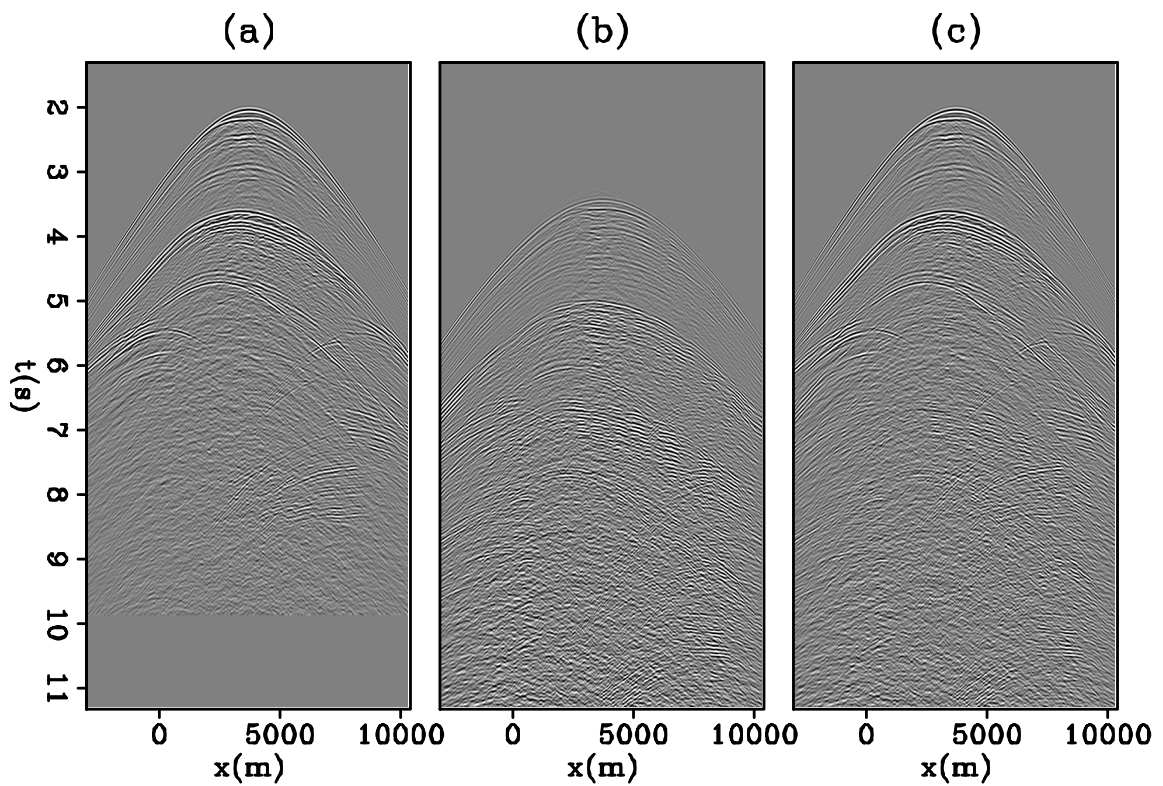


Figure 5.4: A receiver gather along the inline direction. (a) shows the mirror reflection energy.(b) shows the double-mirror reflection energy. (c) shows the total down-going energy, which is generated by the sum of (a) and (b). [ER] chap5/. chap5-data

The second inversion has an operator that accounts for the kinematics of both the mirror and the double-mirror reflection. Its objective function, $S_{\text{joint}}(\mathbf{m})$, is:

$$S_{\text{joint}}(\mathbf{m}) = \|(\mathbf{L}_{\text{mirror}} + \mathbf{L}_{\text{double}}) \mathbf{m} - \mathbf{d}_{\downarrow}\|^2, \quad (5.2)$$

$$= \|\mathbf{L}_{\downarrow} \mathbf{m} - \mathbf{d}_{\downarrow}\|^2, \quad (5.3)$$

where $\mathbf{L}_{\text{double}}$ represents the Born forward modeling operator for the double-mirror reflection. The sum of $\mathbf{L}_{\text{mirror}}$ and $\mathbf{L}_{\text{double}}$ becomes \mathbf{L}_{\downarrow} , which represents the Born forward modeling operator that accounts for both the mirror and the double-mirror reflection. In general, the computational cost of applying \mathbf{L}_{\downarrow} is the same as the computational cost of applying $\mathbf{L}_{\text{mirror}}$. However, joint LSRTM is applied to a longer recording time to capture some of the later arrivals from the double-mirror reflection. Therefore, the computational cost scales linearly with the number of time steps in the finite difference time-domain calculation. I use 10 iterations of conjugate direction to perform the two inversions. To speed up convergence, I have applied some techniques introduced in Chapter 3. In the next section, I will discuss some of the preparation I made before initiating the inversion.

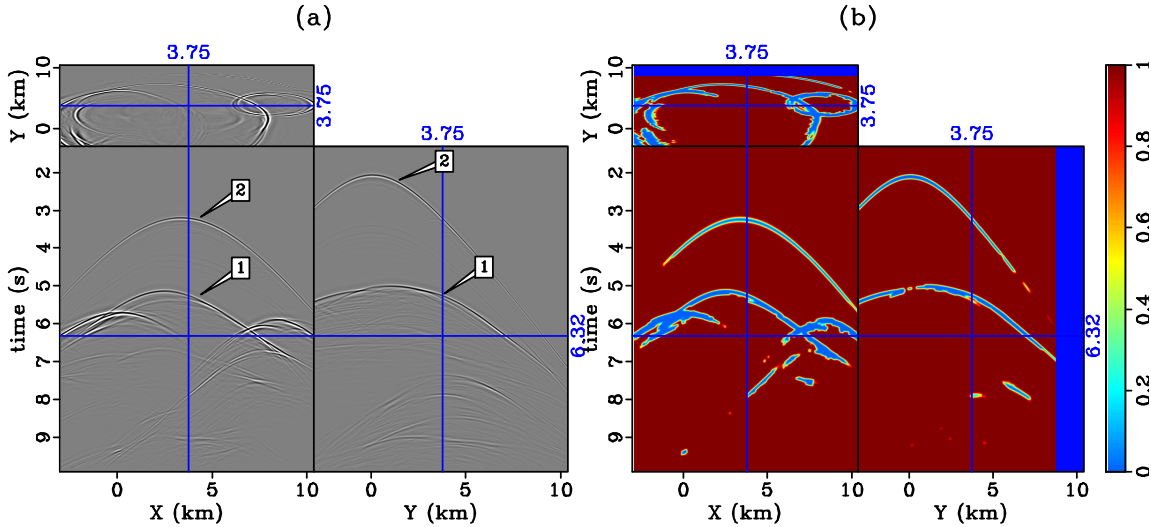


Figure 5.5: (a) Born modeled data using the migration velocity model for an ocean-bottom node located at $x=3300\text{m}$ and $y=25\text{m}$. (b) The corresponding data-weighting function used for salt dimming. [CR] chap5/. chap5-dim

PREPARATION FOR INVERSION

In this dataset, the salt reflection energy is relatively strong when compared to other reflection energy. I included salt dimming, as introduced in Chapter 3, to the LSRTM algorithm. Salt dimming aims to down-weight the contribution of strong reflection energy that corresponds to the sharp velocity contrast in the background (migration) velocity model.

The motivation is to allow the inversion to fit other parts of the image quickly with the fewest number of iterations possible. For LSRTM to perform properly, a sufficiently good migration velocity model that is close to the true velocity model is needed. Later, I will examine how LSRTM performs in areas with velocity errors. The objective functions with salt dimming become:

$$S_{\text{mirror}}(\mathbf{m}) = \|\mathbf{W}_{\text{mirror}}^s(\mathbf{L}_{\text{mirror}}\mathbf{m} - \mathbf{d}_{\downarrow})\|^2, \quad (5.4)$$

$$S_{\text{joint}}(\mathbf{m}) = \|\mathbf{W}_{\downarrow}^s(\mathbf{L}_{\downarrow}\mathbf{m} - \mathbf{d}_{\downarrow})\|^2, \quad (5.5)$$

where $\mathbf{W}_{\text{mirror}}^s$ and $\mathbf{W}_{\downarrow}^s$ represent the salt-dimming data weighting function for the mirror and the down-going signal, respectively. Figure 5.5a shows the Born modeled data for the mirror reflection of an OBN located at $x=3300\text{m}$ and $y=25\text{m}$. In Figure 5.5a, the energy from the top-of-salt reflection arrives at around $t=5\text{s}$ as shown by label 1. There is also strong energy arriving at an earlier time (label 2), this energy corresponds to the reflection off the sea-bottom. Figure 5.5b shows the corresponding data-weighting function. The salt and seabed reflection energy are down-weighted to a value of 0.1. The energy coming from the bottom-of-salt reflection is not affected, because it is relatively weak in the data.

Besides salt dimming, I also applied data reweighting, introduced in Chapter 3, to emphasize the shadow zone in the subsurface. I allow the inversion to fit the shallower part of the data for a few iterations and then reweight the entire inversion to focus onto the deeper part. Due to the complexity of this model, I applied two sets of data reweighting that correspond to two different poorly illuminated areas.

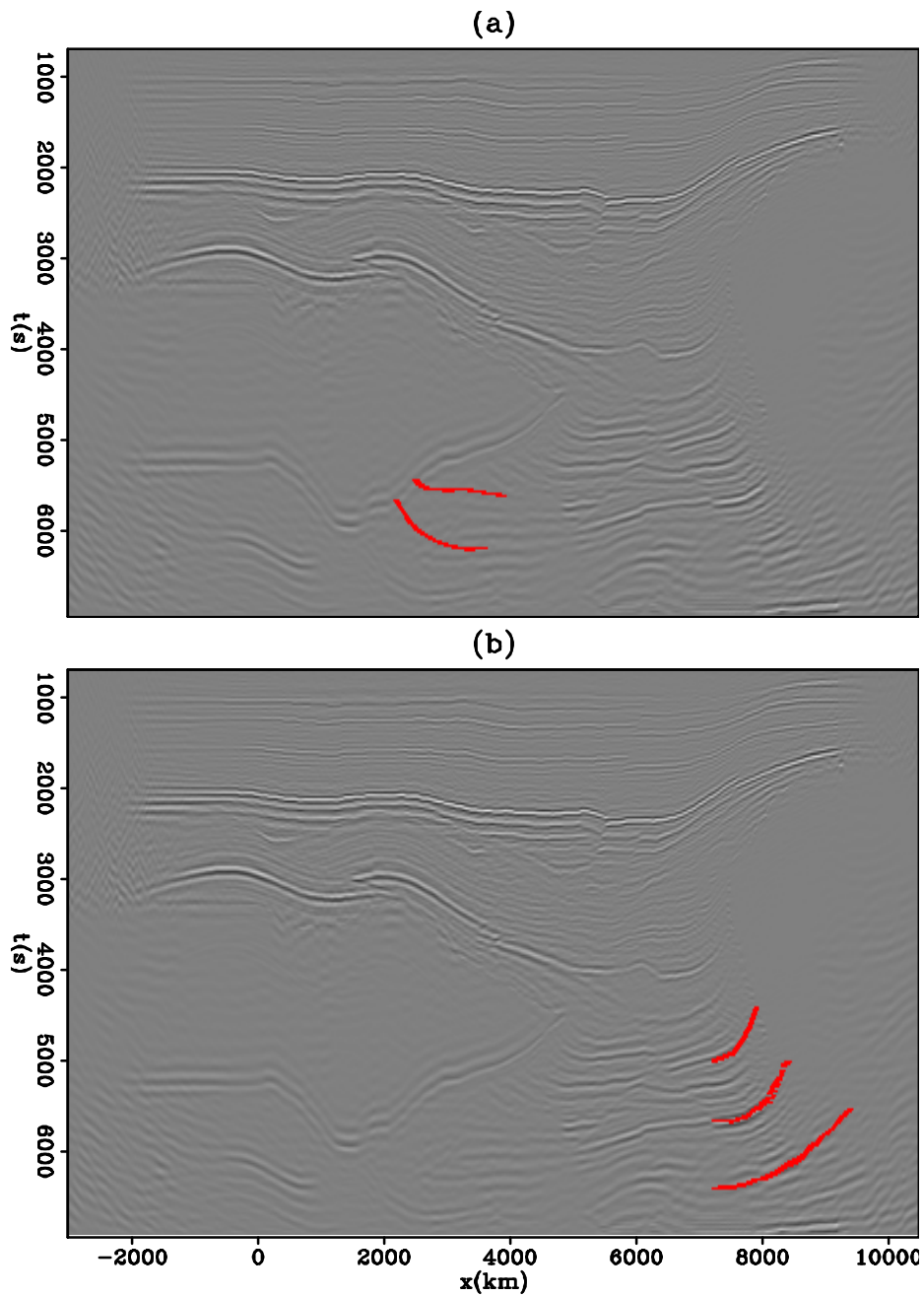


Figure 5.6: Reflector picks used to generate data reweighting. (a) shows the picks from the left subsalt area. (b) shows the picks from the right subsalt areas. I performed the picking over many inline sections and these picks are interpolated as a plane along the crossline direction. [CR] `chap5/. chap5-pick`

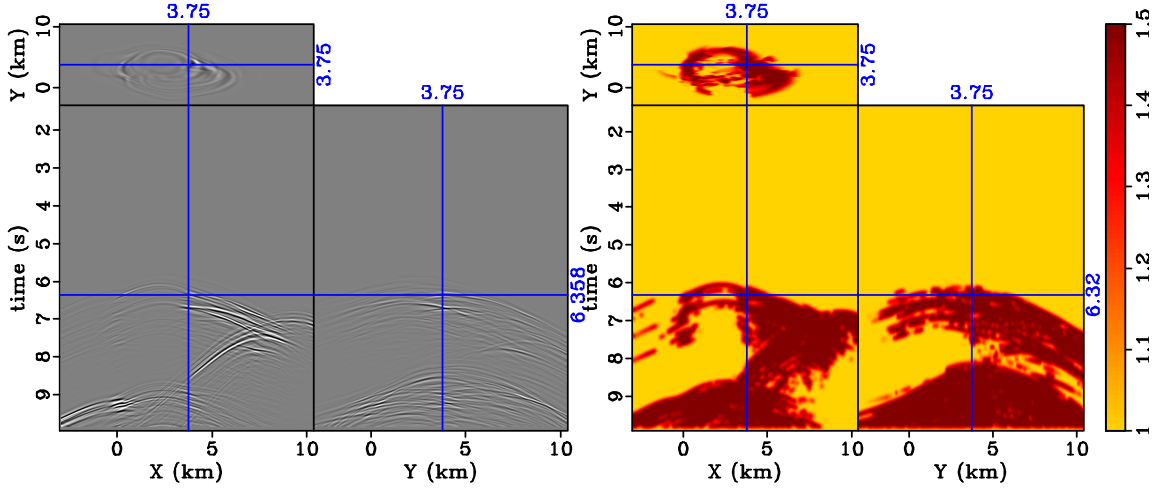


Figure 5.7: (a) Born-modeled data of the picked reflectors in Figure 5.6a and (b) the associated data weighting. The weighting is calculated by an envelope around the prominent energy in the Born modeled data. [CR] `chap5/. chap5-bright`

Figure 5.6a shows the picked reflectors (in red) underneath the left salt structure. Similarly, Figure 5.6b shows the picked reflectors (in red) underneath the right salt structure. I used the OpenCPS seismic processing software to perform the picking over many inline sections. The software then interpolates along the crossline direction and outputs my picks as a plane.

Next, I perform Born modeling of the picked reflectors (Figure 5.7a) and then extract an envelope around the forward modeled energy to produce a diagonal data weighting function (Figure 5.7b). The objective functions for the two inversions become,

$$S_{\text{mirror}}(\mathbf{m}) = \begin{cases} \|\mathbf{W}_{\text{mirror}}^s(\mathbf{L}_{\text{mirror}}\mathbf{m} - \mathbf{d}_{\downarrow})\|^2 & : I_{\text{iter}} < n_{rw1} \\ \|\mathbf{W}_{\text{mirror}}^{B1}\mathbf{W}_{\text{mirror}}^s(\mathbf{L}_{\text{mirror}}\mathbf{m} - \mathbf{d}_{\downarrow})\|^2 & : n_{rw1} \leq I_{\text{iter}} < n_{rw2} \\ \|\mathbf{W}_{\text{mirror}}^{B2}\mathbf{W}_{\text{mirror}}^s(\mathbf{L}_{\text{mirror}}\mathbf{m} - \mathbf{d}_{\downarrow})\|^2 & : I_{\text{iter}} \geq n_{rw2}, \end{cases}$$

$$S_{\text{joint}}(\mathbf{m}) = \begin{cases} \|\mathbf{W}_{\downarrow}^s(\mathbf{L}_{\downarrow}\mathbf{m} - \mathbf{d}_{\downarrow})\|^2 & : I_{\text{iter}} < n_{rw1} \\ \|\mathbf{W}_{\downarrow}^{B1}\mathbf{W}_{\downarrow}^s(\mathbf{L}_{\downarrow}\mathbf{m} - \mathbf{d}_{\downarrow})\|^2 & : n_{rw1} \leq I_{\text{iter}} < n_{rw2} \\ \|\mathbf{W}_{\downarrow}^{B2}\mathbf{W}_{\downarrow}^s(\mathbf{L}_{\downarrow}\mathbf{m} - \mathbf{d}_{\downarrow})\|^2 & : I_{\text{iter}} \geq n_{rw2}, \end{cases}$$

where $\mathbf{W}_{\downarrow}^{B1}$ and $\mathbf{W}_{\downarrow}^{B2}$ are the down-going data weightings that emphasize poorly illuminated areas underneath the right and the left salt structures, respectively. $\mathbf{W}_{\text{mirror}}^{B1}$ and $\mathbf{W}_{\text{mirror}}^{B2}$ are similar to $\mathbf{W}_{\downarrow}^{B1}$ and $\mathbf{W}_{\downarrow}^{B2}$, except that they account for the kinematics of the mirror reflection instead of the down-going reflection. I_{iter} is the current iteration number in the conjugate direction scheme. n_{rw1} and n_{rw2} are the iteration limits that mark the transition between different data weightings. I used $n_{rw1} = 4$ and $n_{rw2} = 8$ as the reweighting limits for this dataset.

RESULTS

By supplying an operator with the proper kinematics to model the down-going data, the main goal of joint inversion is to achieve the following:

1. Crosstalk suppression
2. Illumination improvement

In the next two sections, I will show a few areas in the image where I observe crosstalk suppression and illumination improvement.

Crosstalk suppression

Figures 5.8a and 5.8b show the image cube from the mirror RTM at a depth of $z=1075\text{m}$ and $z=2000\text{m}$. In the figure, the pattern in the shallower depth section (Figure 5.8a) is repeated as an imprint in the deeper depth section (Figure 5.8b). This is the result of crosstalk artifacts from migrating the double-mirror reflection energy with the kinematics of the mirror RTM operator. The same kind of crosstalk artifacts can be found in the joint LSRTM. Figure 5.9 shows the same depth section

as in Figure 5.8b from the joint LSRTM at iteration 1, 4, and 10. Notice that the imprint has been gradually removed by the inversion algorithm.

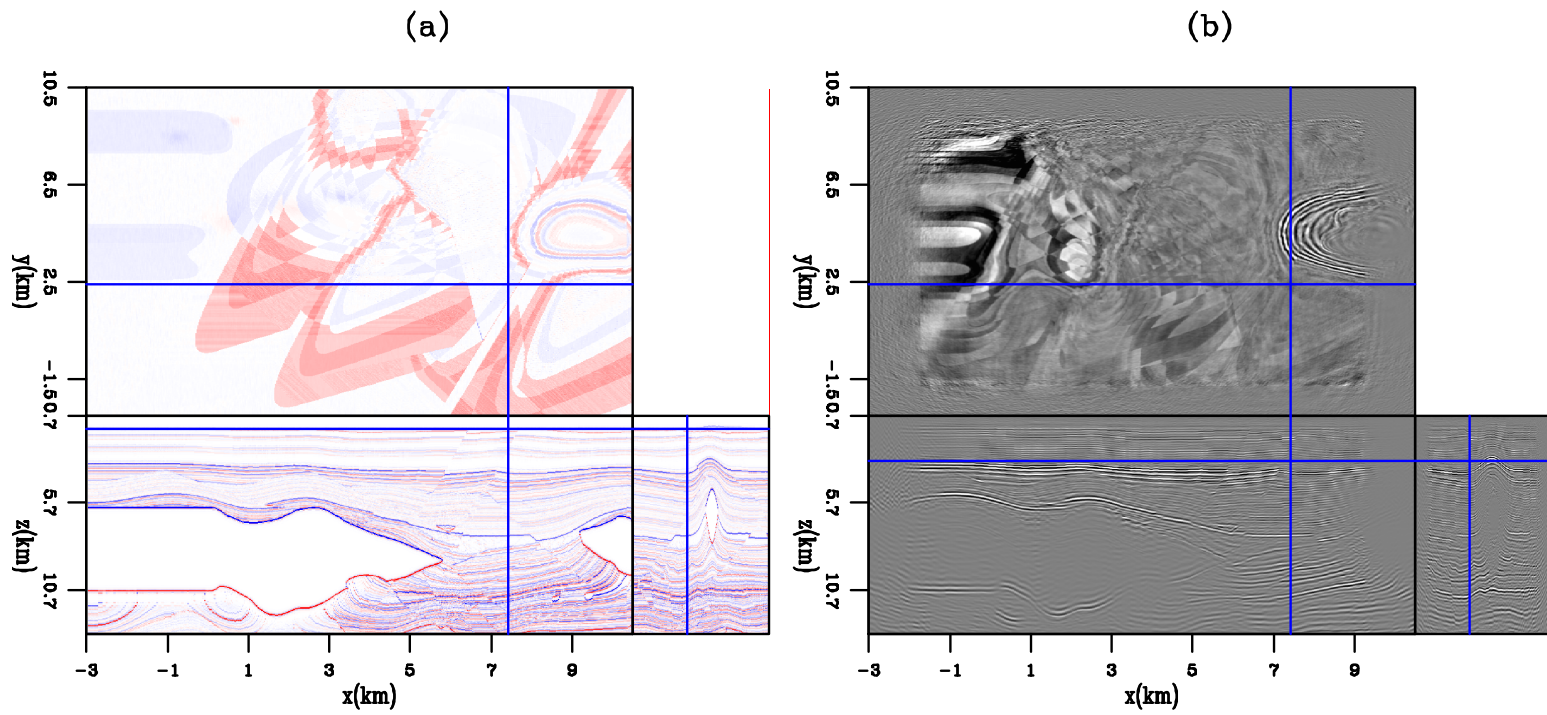


Figure 5.8: The image cube calculated using mirror RTM. The top panels show the depth section extracted at (a) $z=1075\text{m}$ and (b) $z=2000\text{m}$. The depth pattern in the shallower section (a) can be found as an imprint in the deeper section (b). This is the result of migrating the double-mirror data with the mirror operator. [CR]

chap5/. chap5-xtalk

Figure 5.10 shows another example of crosstalk artifacts appearing in the migration image. The annotations point to areas inside the salt where there are spurious reflectors. These spurious reflectors are the result of applying the mirror migration operator onto the double-mirror data. In Figure 5.10b, the coherent energy that forms the crosstalk artifacts has been suppressed by the joint-LSRTM algorithm.

Illumination improvement

Beside crosstalk suppression, joint-LSRTM can also enhance the subsurface illumination of the image by including the double-mirror reflection energy as signal. There are a few areas in the mirror RTM image that are poorly illuminated. Usually, those regions are close to or underneath a complex salt structure. The double-mirror reflection has an equivalent geometry of a dense source and receiver arrays. As a result, some of the double-mirror reflection energy can better reach these poorly illuminated areas.

Figure 5.11a, b, and d show a crossline section calculated using three different techniques. They are mirror RTM with spectral balancing, mirror LSRTM, and joint LSRTM. The reflectivity model (Figure 5.11c) is also included for comparison. Label A points to a salt structure. The areas near and underneath the salt structure are poorly illuminated (Circle B). When I perform mirror LSRTM (Figure 5.11b), we can see an improvement in this region. However, joint LSRTM (Figure 5.11d) can further improve the image because the double-mirror reflection energy are also used as signal. The reflectors that terminate against the salt are better delineated. In addition, the anticline below the salt becomes more interpretable. Circle C highlights a region where the sediment laying on top of the salt body is better imaged with joint LSRTM than with the other techniques.

Figure 5.12a, b, and d show an inline section calculated using three different techniques. They are mirror RTM with spectral balancing, mirror LSRTM, and joint LSRTM. Circle A shows a region against the right salt flank that is poorly illuminated. Label B points to an area where the reflectors near the salt flank are

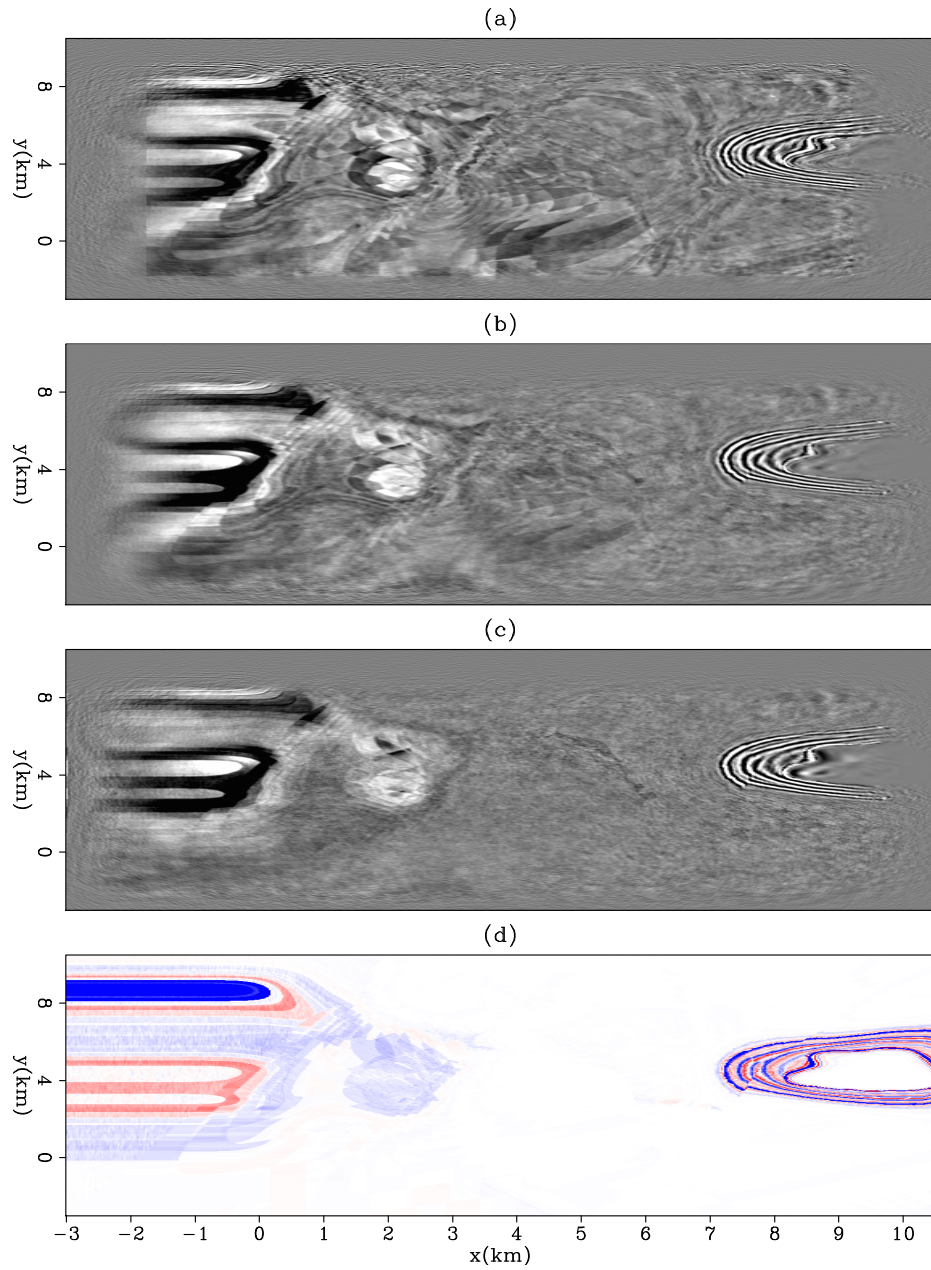


Figure 5.9: The depth section at $z=2000\text{m}$ from the joint LSRTM image at (a) iteration 1, (b) iteration 4, and (c) iteration 10. (d) shows the reflectivity model.

[CR] chap5/. chap5-xtalk-iter

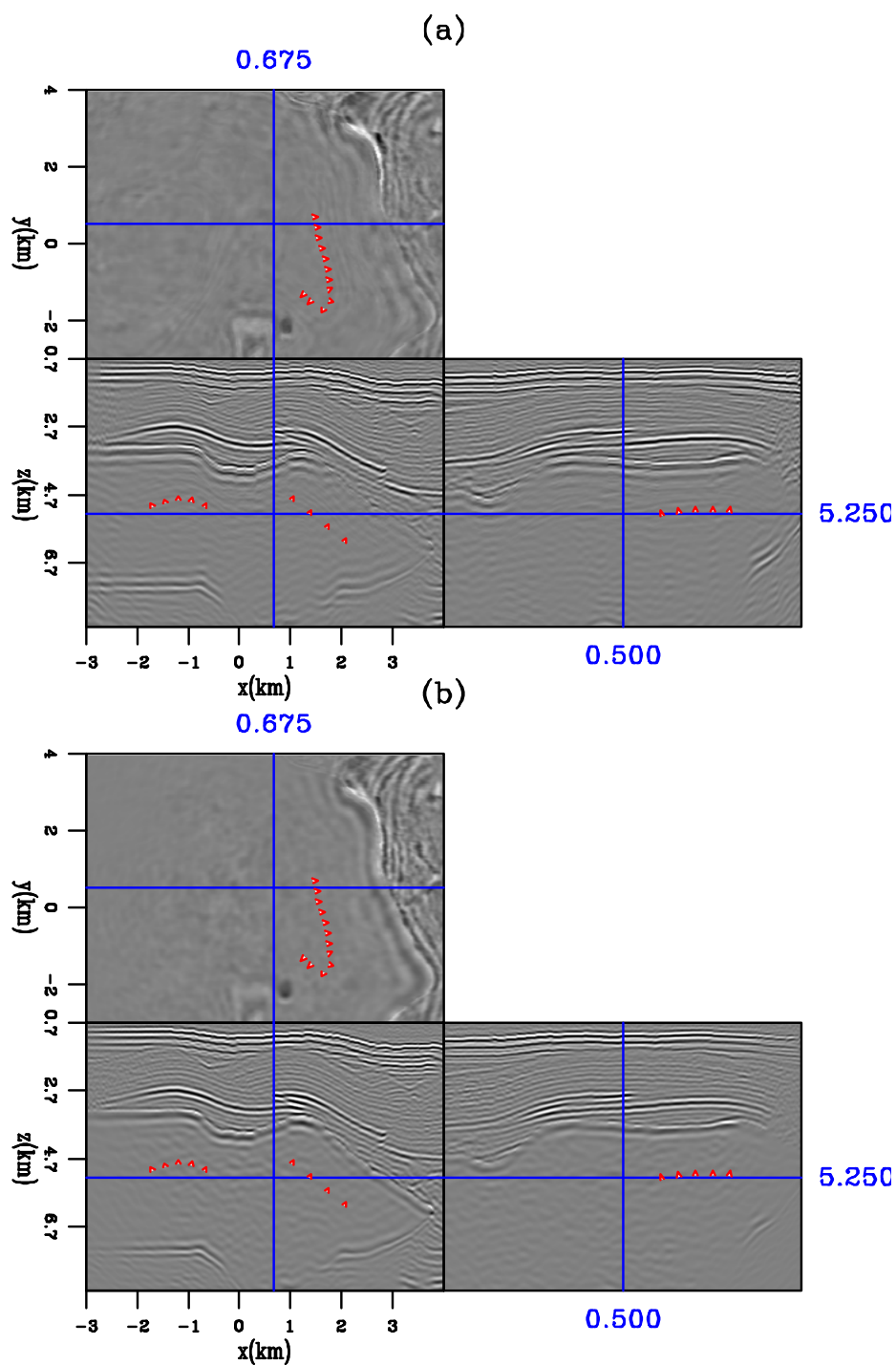


Figure 5.10: (a) The image cube calculated using joint RTM. The arrows point to areas where crosstalk artifacts appear. (b) The image cube calculated after 10 iterations of joint-LSRTM. Notice the crosstalk artifacts have been suppressed. [CR]

chap5/. chap5-xtalk-salt

better illuminated with joint LSRTM. In addition, there are some conflicting dips in the image with energy oriented almost perpendicularly to the direction of the true reflectors. These noises are better suppressed by joint LSRTM.

Figure 5.13 shows an example where the base of salt is better imaged with joint LSRTM. When only the mirror signal is used (Figure 5.13a and 5.13b), the base-of-salt boundary in circle A and circle B is not well defined. In the joint LSRTM image (Figure 5.13d), the base-of-salt boundary is more coherent and becomes more interpretable.

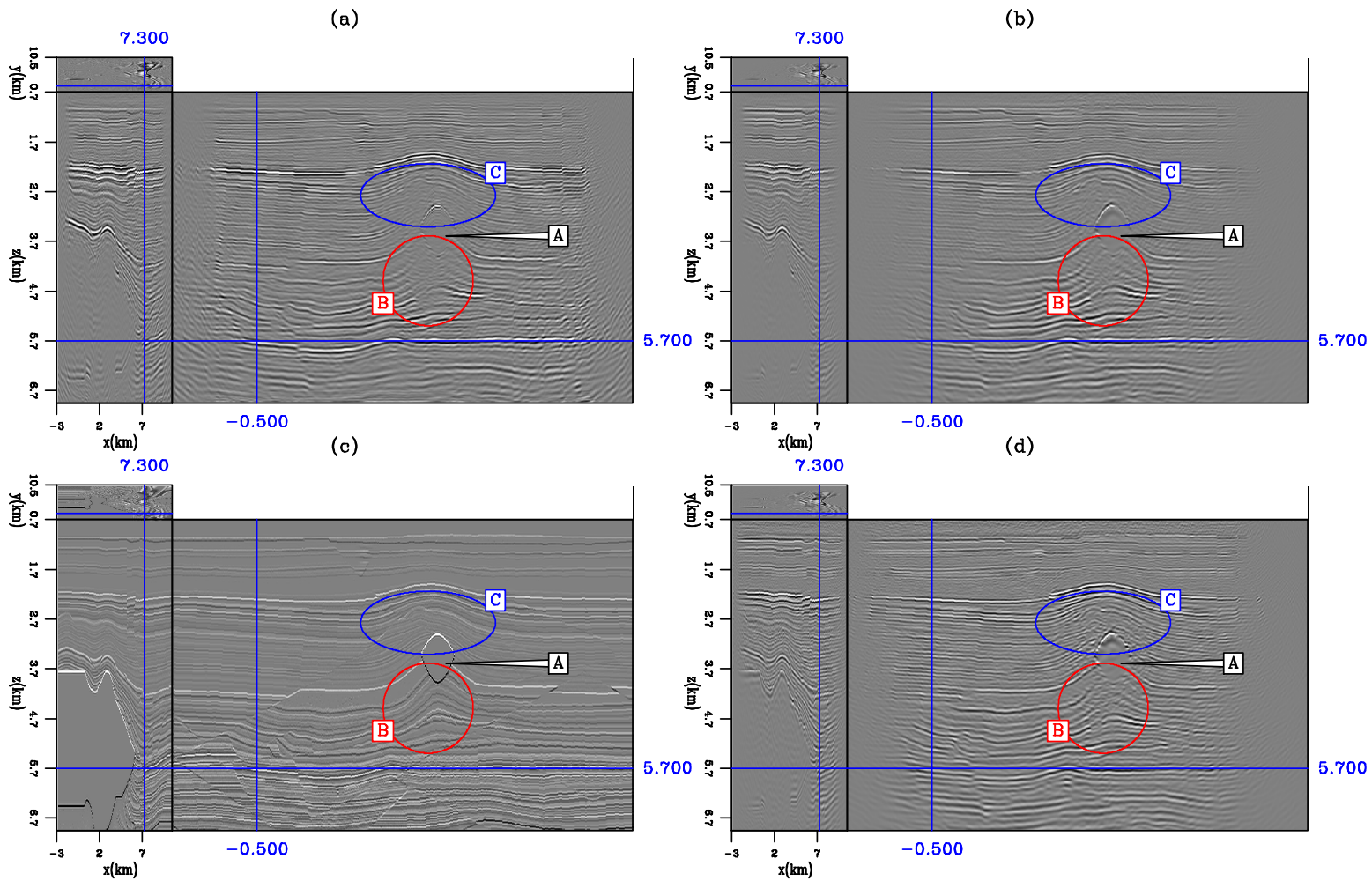


Figure 5.11: A crossline section calculated using (a) mirror RTM with spectral balancing, (b) mirror LSRTM, (c) true model, and (d) joint LSRTM. The regions around the salt body (label A) are poorly illuminated. Circle B and C show area of improvement when using joint LSRTM as compared to the other techniques. [CR]

chap5/. chap5-enhance1

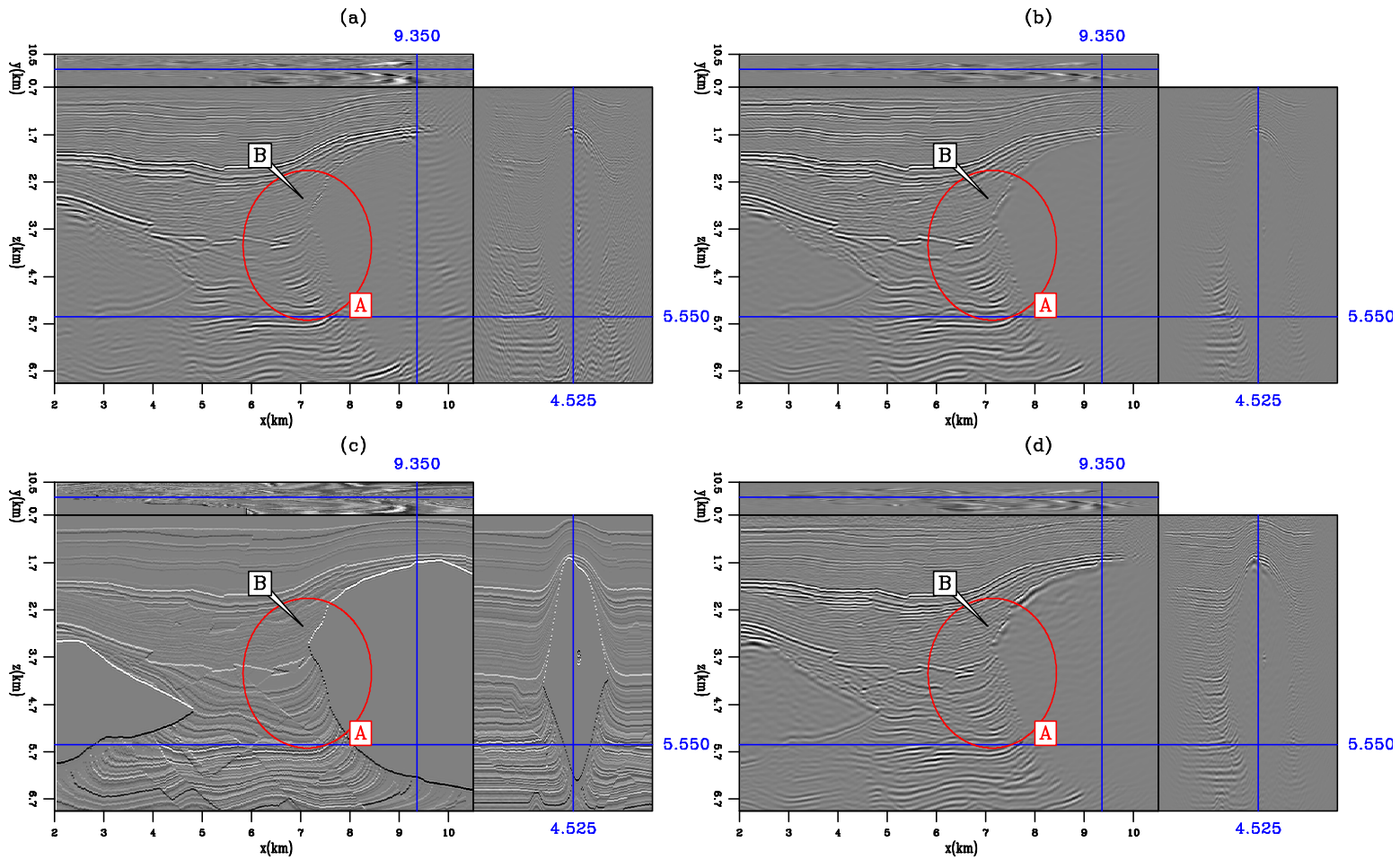


Figure 5.12: An inline section calculated using (a) mirror RTM with spectral balancing, (b) mirror LSRTM, (c) true model, and (d) joint LSRTM. The regions around the salt body (label A) are poorly illuminated. Label B points to an area where the reflector near the salt flank are better illuminated. [CR] chap5/. chap5-enhance2

CONCLUSION

In this chapter, I extend the methodology for imaging with surface-related multiples using joint LSRTM to a 3D data example. The physics in the LSRTM operator properly account for both the first order (mirror) and higher order (double-mirror) reflections. Therefore, we observe crosstalk reduction and illumination improvement in the image. In particular, areas near and underneath a complex salt structure are better illuminated with joint LSRTM. In an OBN survey, receivers are sparsely placed and surface-related multiple elimination can be a challenging task. Joint LSRTM eliminates the need to separate out surface-related multiples in the down-going data and can be a viable alternative to traditional processing.

ACKNOWLEDGMENTS

I thank the Stanford Center for Computational Earth & Environmental Science (CEES) for providing the computer resources used in these studies. I acknowledge Open Geophysical, Inc., a Dolphin Geophysical Company, for providing the OpenCPS software. I am grateful to Stew Levin for teaching me how to use the OpenCPS software. I acknowledge Bob Clapp for creating the dataset and Chris Leader for providing the GPU codes to generate the dataset. I thank Ohad Barak for generating the 3D salt model and I appreciate the input from Biondo Biondi and Shuki Ronen.

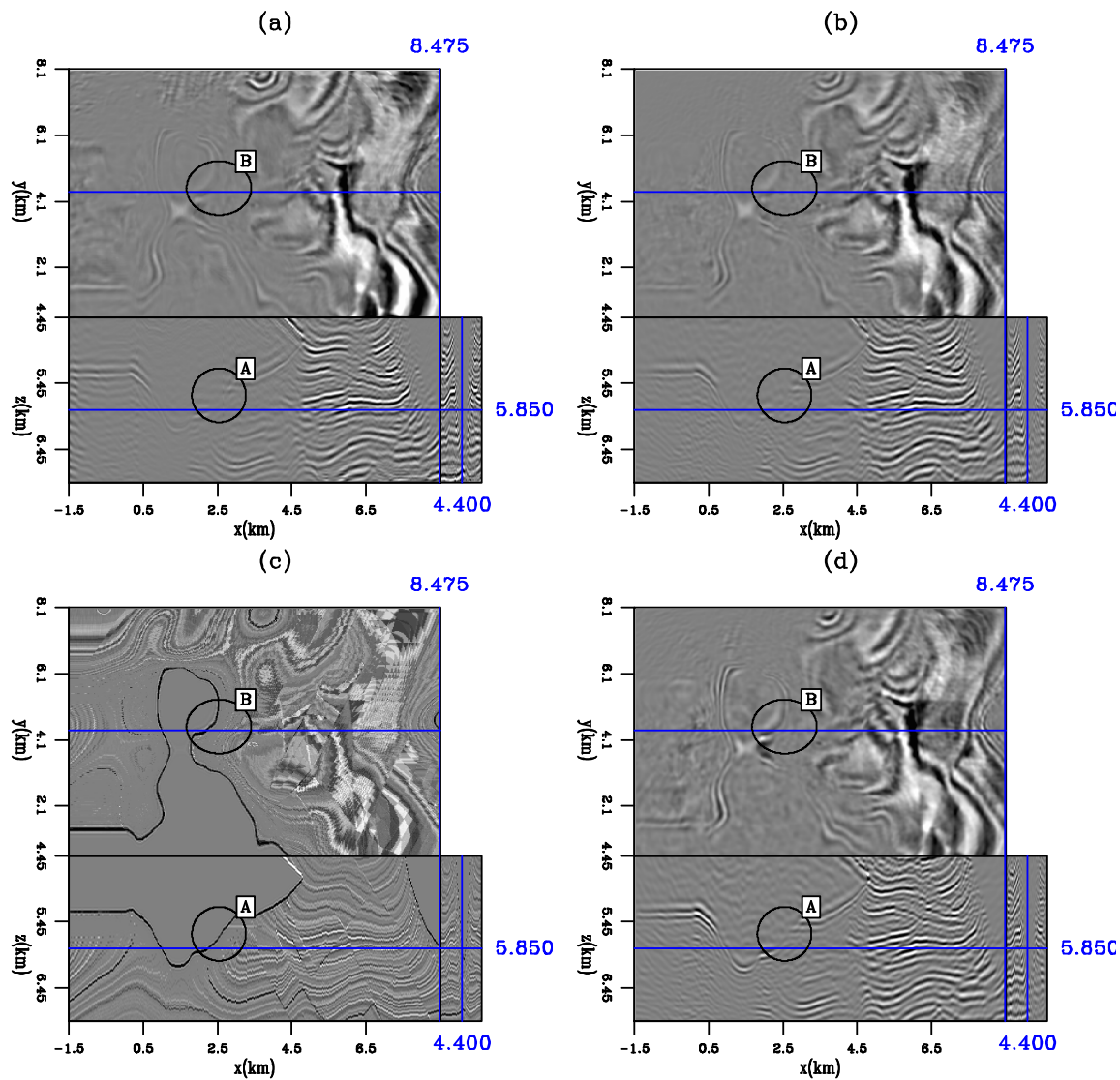


Figure 5.13: Image cubes extracted at $x=8475\text{m}$, $y=4400\text{m}$ and $z=5850\text{m}$. (a) Mirror RTM with spectral balancing, (b) mirror LSRTM, (c) true model, and (d) joint LSRTM. The base-of-salt boundary is more coherent and better defined with joint LSRTM. [CR] chap5/. chap5-enhance3